

# UCLA

## UCLA Previously Published Works

### Title

Acid-Base Control of Valency within Carboranedithiol Self-Assembled Monolayers: Molecules Do the Can-Can

### Permalink

<https://escholarship.org/uc/item/45f5c9j0>

### Journal

ACS Nano, 12(3)

### ISSN

1936-0851

### Authors

Thomas, John C  
Goronzy, Dominic P  
Serino, Andrew C  
[et al.](#)

### Publication Date

2018-03-27

### DOI

10.1021/acsnano.7b09011

Peer reviewed

## Acid-Base Control of Valency within Carboranedithiol Self-Assembled Monolayers: Molecules Do the Can-Can

John C. Thomas, Dominic P Goronzy, Andrew C. Serino, Harsharn S Auluck, Olivia R Irving, Elisa Jimenez-Izal, Jacqueline Deirmenjian, Jan Machacek, Philippe Sautet, Anastassia N. Alexandrova, Tomas Base, and Paul S. Weiss

ACS Nano, **Just Accepted Manuscript** • DOI: 10.1021/acsnano.7b09011 • Publication Date (Web): 02 Feb 2018

Downloaded from <http://pubs.acs.org> on February 13, 2018

### Just Accepted

“Just Accepted” manuscripts have been peer-reviewed and accepted for publication. They are posted online prior to technical editing, formatting for publication and author proofing. The American Chemical Society provides “Just Accepted” as a service to the research community to expedite the dissemination of scientific material as soon as possible after acceptance. “Just Accepted” manuscripts appear in full in PDF format accompanied by an HTML abstract. “Just Accepted” manuscripts have been fully peer reviewed, but should not be considered the official version of record. They are citable by the Digital Object Identifier (DOI®). “Just Accepted” is an optional service offered to authors. Therefore, the “Just Accepted” Web site may not include all articles that will be published in the journal. After a manuscript is technically edited and formatted, it will be removed from the “Just Accepted” Web site and published as an ASAP article. Note that technical editing may introduce minor changes to the manuscript text and/or graphics which could affect content, and all legal disclaimers and ethical guidelines that apply to the journal pertain. ACS cannot be held responsible for errors or consequences arising from the use of information contained in these “Just Accepted” manuscripts.



1  
2  
3  
4  
5  
6  
7  
8  
9  
10  
11  
12  
13  
14  
15  
16  
17  
18  
19  
20  
21  
22  
23  
24  
25  
26  
27  
28  
29  
30  
31  
32  
33  
34  
35  
36  
37  
38  
39  
40  
41  
42  
43  
44  
45  
46  
47  
48  
49  
50  
51  
52  
53  
54  
55  
56  
57  
58  
59  
60

# Acid-Base Control of Valency within Carboranedithiol Self-Assembled Monolayers: Molecules Do the Can-Can

John C. Thomas,<sup>1,2</sup> Dominic P. Goronzy,<sup>1,2</sup> Andrew C. Serino,<sup>2,3</sup> Harsharn S. Auluck,<sup>1,2</sup>  
Olivia R. Irving,<sup>1</sup> Elisa Jimenez-Izal,<sup>1,4</sup> Jacqueline M. Deirmenjian,<sup>1,2</sup> Jan Macháček,<sup>5</sup>  
Philippe Sautet,<sup>1,2,6</sup> Anastassia N. Alexandrova,<sup>\*1,2</sup> Tomáš Baše,<sup>\*5</sup> and Paul S. Weiss<sup>\*1,2,3</sup>

<sup>1</sup>Department of Chemistry and Biochemistry, University of California, Los Angeles, Los Angeles, CA 90095, United States

<sup>2</sup>California NanoSystems Institute, University of California, Los Angeles, Los Angeles, CA 90095, United States

<sup>3</sup>Department of Materials Science and Engineering, University of California, Los Angeles, Los Angeles, CA 90095, United States

<sup>4</sup>Kimika fakultatea, Euskal Herriko Unibertsitatea (UPV/EHU), and Donostia International Physics Center (DIPC), P. K. 1072, 20080 Donostia, Euskadi, Spain

<sup>5</sup>Institute of Inorganic Chemistry of the Czech Academy of Sciences, 250 68 Husinec-Řež, č. p.

1  
2  
3 1001, Czech Republic  
4  
5

6 <sup>6</sup>Department of Chemical and Biomolecular Engineering, University of California, Los Angeles,  
7  
8 Los Angeles, CA 90095, United States  
9  
10

11  
12 \*Address correspondence to: psw@cnsi.ucla.edu (P.S.W.), tbase@iic.cas.cz (T.B.),  
13  
14 ana@chem.ucla.edu (A.A.)  
15  
16  
17  
18  
19

## 20 **KEYWORDS**

21  
22 nanoscience, self-assembly, carborane, self-assembled monolayer, dipoles, scanning tunneling  
23  
24 microscopy, two dimensional, molecular switch  
25  
26  
27  
28  
29  
30  
31  
32  
33  
34  
35  
36  
37  
38  
39  
40  
41  
42  
43  
44  
45  
46  
47  
48  
49  
50  
51  
52  
53

**ABSTRACT**

We use simple acid-base chemistry to control the valency in self-assembled monolayers of two different carboranedithiol isomers on Au{111}. Monolayer formation proceeds *via* Au-S bonding, where manipulation of pH prior to or during deposition enables the assembly of dithiolate species, monothiol/monothiolate species, or combination. Scanning tunneling microscopy (STM) images identify two distinct binding modes in each unmodified monolayer, where simultaneous spectroscopic imaging confirms different dipole offsets for each binding mode. Density functional theory calculations and STM image simulations yield detailed understanding of molecular chemisorption modes and their relation with the STM images, including inverted contrast with respect to the geometric differences found for one isomer. Deposition conditions are modified with controlled equivalents of either acid or base, where the coordination of the molecules in the monolayers is controlled by protonating or deprotonating the second thiol/thiolate on each molecule. This control can be exercised during deposition to change the valency of the molecules in the monolayers, a process that we affectionately refer to as the “can-can.” This control enables us to vary the density of molecule-substrate bonds by a factor of two without changing the molecular density of the monolayer.

1  
2  
3  
4  
5  
6  
7  
8  
9  
10  
11  
12  
13  
14  
15  
16  
17  
18  
19  
20  
21  
22  
23  
24  
25  
26  
27  
28  
29  
30  
31  
32  
33  
34  
35  
36  
37  
38  
39  
40  
41  
42  
43  
44  
45  
46  
47  
48  
49  
50  
51  
52  
53

Self-assembled monolayer (SAM) formation is driven by a combination of substrate-molecule interactions, molecule-molecule interactions, and molecule-environment interactions.<sup>1-3</sup> The most commonly studied SAMs, *n*-alkanethiolates on Au{111} contain a single thiol group available for substrate binding, have linear backbones, resulting in numerous defects that originate from *gauche* defects in the alkyl chains, different alkyl tilt orientations, translational and rotational lattice registry offsets, and reconstruction of the underlying substrate.<sup>1,4-9</sup> Monolayers formed from dialkyl disulfides on Au{111} result in identical assemblies as the Au surface cleaves the S-S bond.<sup>10-12</sup> In contrast, in unfunctionalized carboranethiol SAMs, the molecules do not tilt nor can they change their conformation; thus, there are fewer and simpler defects in comparison to SAMs composed of *n*-alkanethiols.<sup>2-17</sup> Interactions between carboranethiol molecules at both exposed and buried interfaces have been observed. Carboranethiol isomers with nonzero components of their dipoles parallel to the surface exhibit long-range attractive interactions due to dipole alignment.<sup>18</sup> This phenomenon was previously inferred from the results of competitive adsorption experiments, where carboranethiol isomers with larger in-plane dipole components outcompeted those with greater out-of-plane components.<sup>19</sup> Mixed assemblies of carboranethiol isomers can be used to tailor the effective metal work function of noble metal surfaces while *not* changing the wetting properties of the overlying polymers and thus not changing their morphologies.<sup>15,20</sup> These interactions have been observed with submolecular resolution, where correlations between simultaneously acquired scanning tunneling microscopy (STM) topographic and local barrier height (LBH) images

1  
2  
3 enabled the observation of single-molecule orientations within SAM matrices and demonstrated  
4 defect-tolerant dipole alignment.<sup>16</sup> The surfactants 9,12-carboranedithiol (**9O12**) and 1,2-  
5 carboranedithiol (**1O2**) have been shown to be stable isomers, to functionalize noble metal  
6 surfaces, and to modify effective metal work functions due to oppositely oriented dipoles  
7 originating from the carborane backbone.<sup>21-26</sup> Carboranethiol SAMs can also be used to align  
8 overlying liquid crystal orientations.<sup>27</sup> Here, both isomers of carboranedithiol studied (**1O2** and  
9 **9O12**) promote formations with higher sulfur-surface coverage and fewer defects due to rigid,  
10 nearly spherical backbones.  
11  
12  
13  
14  
15  
16  
17  
18  
19  
20  
21  
22

23 Typical SAM formation from thiols is governed by simple acid-base reactions, where an  
24 acidic thiol group (SH) is deprotonated to a thiolate (S<sup>-</sup>) on reactive surfaces.<sup>4,28</sup> As noted above,  
25 disulfides can form SAMs by cleaving the disulfide bonds, again leading to adsorbed  
26 thiolates.<sup>10-12</sup> Adsorbed thiolates form stable bonds to Au surfaces (~45 kcal/mol), stronger than  
27 typical Au-Au bonds.<sup>3,29-31</sup> The S-Au bond is partially ionic and partially covalent; the effective  
28 charge transfer depends on the backbone attached to the S.<sup>32</sup> Adsorbed, but relatively labile,  
29 thiols (*i.e.*, with protons still in place) have also been observed within SAMs, such as  
30 *p*-carboranethiol, on Au{111} at low concentrations.<sup>17</sup> The ease of formation coupled with  
31 tunable defect formations contribute towards thin films with controllable intermolecular  
32 interactions and modifiable surface-mediated effects that can be used to advantage to place and  
33 to direct single molecules and supramolecular assemblies into controlled environments.<sup>2,3,12,13,33</sup>  
34  
35 Acid-base chemistry, at the exposed interface, has shown broad importance in surface  
36 wettability, colloid and emulsion stability, biological signal transduction and membrane  
37 assembly, and catalysis.<sup>34-37</sup> We sought to manipulate and to control the valency, the molecule-

1  
2  
3 substrate bond density, and subsequent monolayer formation using different isomers of  
4  
5 carboranedithiol on Au surfaces, both of which have the potential for one *or* two bonds to the  
6  
7 substrate per molecule. Both **1O2** and **9O12** are stable in their respective dithiol and dianion  
8  
9 states, where **1O2** is a stronger acid compared to **9O12**.<sup>26</sup> The acid-base properties intrinsic to  
10  
11 homogenous monolayers composed of either **1O2** or **9O12** can be used as a means of control.  
12  
13  
14

15  
16 Kitagawa and coworkers assembled adamantanetrithiol on Au{111} and found trivalent  
17  
18 interactions that resulted in small chiral cluster structures on the surface.<sup>38</sup> In earlier unpublished  
19  
20 work, we found that it is important to take into account both bond angles and substrate access in  
21  
22 forming multivalent molecule-substrate interactions.<sup>39,40</sup> The lessons learned from those studies  
23  
24 resulted in the inclusion of flexible linkers in attaching caltrops and other molecules to  
25  
26 surfaces.<sup>41-44</sup>  
27  
28  
29

30  
31 Control of thin-film properties of both exposed and buried interfaces has broad  
32  
33 implications, *e.g.*, for molecular devices and lithographic patterning.<sup>3,29,33,35,45,46</sup> These isomers of  
34  
35 *o*-carboranedithiols serve as ideal test candidates for binding, valency, and surface bond density,  
36  
37 where singly bound (monovalent) modes produce monolayers with lower thiolate-Au bond  
38  
39 densities in comparison to doubly bound (divalent) modes. We demonstrate, with a variety of  
40  
41 surface-sensitive techniques and with density functional theory (DFT) calculations, that  
42  
43 homogenous monolayers composed of either **1O2** or **9O12** show two distinct binding states,  
44  
45 which are susceptible to manipulation by controlling pH, in solution, prior to deposition, as well  
46  
47 as during deposition *via* exposure to acidic or basic solution; identical nearest-neighbor spacings  
48  
49 and lattices are maintained throughout processing, independent of valency. We also show that  
50  
51  
52  
53



1  
2  
3 the difference between the monovalent and divalent modes of these carboranes is not a simple  
4  
5 geometric effect, but also critically depends on electronic effects.  
6  
7

8  
9 Scanning tunneling microscopy is able to probe the topographic landscape of surfaces with sub-  
10  
11 Ångström precision.<sup>7,47-50</sup> We have previously used spectroscopic imaging modalities of STM to  
12  
13 probe buried interfaces and layers in molecular monolayers of other systems.<sup>7,16,32,51-55</sup>  
14  
15

## 16 17 **Results and Discussion**

18  
19  
20 We assembled and measured monolayers composed of either **1O2** or **9O12** carboranedithiols on  
21  
22 Au{111}/mica, where, upon imaging, two distinct binding states that differ in apparent height in  
23  
24 each homogenous SAM are recorded (Figure 1). Both isomers form hexagonally close-packed  
25  
26 monolayers with nearest-neighbor spacings of  $7.6 \pm 0.5$  Å. This formation is best explained by a  
27  
28  $(\sqrt{7} \times \sqrt{7})R19.12^\circ$  superstructure that is found for several carboranethiols on Au{111}.<sup>19,56</sup> We  
29  
30 measured a bimodal distribution, with tunable coverages, which we attribute to both singly  
31  
32 bound (monovalent) and doubly bound (divalent) states. Self-assembled monolayers formed of  
33  
34 **1O2** from a neutral solution show  $21 \pm 8\%$  coverage of the singly bound (greater apparent height  
35  
36 in STM images) binding structure and, correspondingly,  $79 \pm 8\%$  coverage of the doubly bound  
37  
38 (lower apparent height) structure. These modes are differentiated as described below.  
39  
40  
41

42  
43 Measurements over monolayers composed of **9O12** show a strong preference ( $98 \pm 1\%$ ) for  
44  
45 monovalent binding (less protruding, counter-intuitively, as explained below) in comparison to  
46  
47 divalent ( $2 \pm 1\%$ , more protruding). Images can be segmented by apparent height in topographic  
48  
49 images by applying a gray scale threshold value that is used to compute binding concentrations  
50  
51 in image binaries (Figure S1). Monovalent structures in **1O2** monolayers have greater apparent  
52  
53

1  
2  
3 heights ( $1.5 \pm 0.3 \text{ \AA}$  with the tunneling conditions and tip used to record the data in Figure 1)  
4  
5 than the divalent structures under the conditions measured; the monovalent structures in **9O12**  
6  
7 SAMs have lower apparent heights ( $0.4 \pm 0.2 \text{ \AA}$  with the tunneling conditions and probe tip used  
8  
9 to record the data in Figure 1) than the divalent structures. The DFT calculations help explain  
10  
11 this apparent inverted contrast for monovalent/divalent modes for **9O12**.  
12  
13  
14

15  
16 We performed DFT calculations to gain detailed understanding of molecular  
17  
18 chemisorption modes and their related appearances in STM images, and to help identify the  
19  
20 adsorbed species. With this aim, we explored all the possible binding sites of singly and doubly  
21  
22 dehydrogenated (*i.e.*, monovalent and divalent, respectively) carboranedithiols on the Au{111}:  
23  
24 face-centered cubic (fcc), hexagonally close-packed (hcp), over a bridge, and over a single atom  
25  
26 (atop). The most stable species that are most closely correlated with the experimental results are  
27  
28 shown in Figure 2. The geometric features of **1O2** and **9O12** are almost identical. The preferred  
29  
30 binding site for the monovalent molecules is a fcc hollow site, which allows them to maximize  
31  
32 the number of Au-S bonds. Divalent species adsorb preferentially on one fcc and one hcp hollow  
33  
34 site, although somewhat off center towards the bridge site. Overall, S-Au bond-lengths are  
35  
36 calculated to be between 2.37 and 3.06  $\text{\AA}$ . The natural bond order analysis shows that these are  
37  
38 predominantly covalent bonds. For the most stable monovalent chemisorption mode, the S-C or  
39  
40 S-B bond is simply normal to the surface. If one defines the molecular axis as connecting the  
41  
42 center of the cage and the point halfway from one S atom to another, this line then is 28-30° from  
43  
44 the surface normal in the monovalent binding mode. The z (surface normal) coordinates of the  
45  
46 uppermost atoms (excluding H), also shown in Figure 2, reveal that the monovalent structures in  
47  
48  
49  
50  
51  
52  
53

1  
2  
3 both **102** and **9012** extend further from the surface than their corresponding divalent species,  
4  
5 each with a physical height difference of *ca.* 0.4 Å  
6  
7

8  
9 The simulated STM images for these four structures are shown in Figure 3. In agreement  
10  
11 with experiments and in line with the geometry, monovalent **102** appears more protruding in  
12  
13 STM images than divalent **102**. The calculated apparent height difference in the simulated STM  
14  
15 images is 0.6 Å. For STM images of **9012**, however, the situation is different; the monovalent  
16  
17 mode appears *less* protruding, while the divalent structure appears more protruding. The height  
18  
19 difference in the simulated images is 0.3 Å. As mentioned above, the z coordinates of the  
20  
21 topmost atoms are higher in the monovalent than in the divalent **9012**. These results indicate that  
22  
23 electronic effects play important roles in these systems and are critical to explain the differences  
24  
25 between images of monovalent and divalent **102** and **9012** on Au{111}.  
26  
27  
28  
29

30  
31 In order to understand this “inverted contrast” in the STM images for **9012**, we  
32  
33 additionally plot the charge densities within the same energy window captured by the STM (from  
34  
35 the Fermi energy ( $E_f$ ) to ( $E_f - 0.1$  eV)). From the images in Figure 4, we observe that the  
36  
37 contributions of C and B in these states are quite similar for monovalent and divalent **102**  
38  
39 structures. Indeed, the relative apparent heights and the relative geometrical heights correlate  
40  
41 well. For **9012**, the charge density plots for monovalent and divalent modes are significantly  
42  
43 different. In the case of the monovalent structure, the contributions of the carborane cage atoms  
44  
45 in the proximity of the Fermi level are significantly smaller, which gives rise to the calculated  
46  
47 “inverted contrast”. The density plots in Figure 4 reflect the collective contributions of all  
48  
49 electronic states that fall within the experimentally measured energy window ( $E_F - 0.1$  eV).  
50  
51  
52  
53

1  
2  
3 Examination of the electronic states and their energies across the entire Brillouin zone reveal that  
4 there are only a few (1-3) of these states for each species. Furthermore, for the monovalent  
5  
6 **9O12**, there is essentially only a single experimentally accessible state, the least among all  
7  
8 considered adsorbed molecules. The projected density of states (PDOS) plots (reported in the  
9  
10 Supplemental Information) are consistent with this finding. Since carboranes, in general, have  
11  
12 similar delocalized chemical bonding, described by Lipscomb *via* three-center, two-electron  
13  
14 bonds, and obey Wade's electron-counting rules,<sup>57</sup> it is expected that the molecular orbitals on all  
15  
16 the studied species are similar in structure, and only shift in energy from one species to another.  
17  
18 Thus, we suggest that the small number of electronic states detected by STM for the monovalent  
19  
20 **9O12** simply has to do with the energies of those states relative to the experimentally probed  
21  
22 energy window of ( $E_F - 0.1$  eV).  
23  
24  
25  
26  
27  
28

29  
30 The aggregation of domains in SAMs composed of **1O2** suggests intermolecular  
31  
32 interactions between monovalent molecules, which possess larger in-plane dipole components  
33  
34 due to binding geometry. The reported dipoles for **1O2** and **9O12** are 3.7 D and 5.5 D,  
35  
36 respectively,<sup>24</sup> where this component is close the surface normal ( $8^\circ$ ) if both S are bound (as  
37  
38 thiolates), however, the singly bound state is tilted  $\sim 30^\circ$  (*vide supra*), yielding a parallel  
39  
40 component ( $\sim 1.8$  D for **1O2** and  $\sim 2.8$  D for **9O12**). This dipole component results in increased  
41  
42 intermolecular interactions between neighboring singly bound adsorbates<sup>16</sup> and apparently leads  
43  
44 to phase separation. This result is confirmed in samples of each monolayer and further enables  
45  
46 binding assignments; SAMs composed of **1O2** demonstrate aggregation between higher  
47  
48 protrusions, and, in SAMs composed of **9O12**, higher intensity protrusions are localized and *not*  
49  
50 phase aggregated. Both isomers form hexagonally close-packed monolayers with nearest-  
51  
52  
53

1  
2  
3 neighbor spacings of  $7.6 \pm 0.5 \text{ \AA}$ . This formation is best explained by a  $(\sqrt{7} \times \sqrt{7})R19.12^\circ$   
4  
5 superstructure that is found for several carboranethiols on Au{111}.<sup>56</sup> One of the advantages of  
6  
7 working with carboranethiol SAMs is the conservation of surface structure among isomers so  
8  
9 that the effects of different interactions can be tested independently of structural variations.<sup>13,19</sup>  
10  
11 Both isomers form monolayers with the same spacings and surface structures; however, each  
12  
13 contains different concentrations of monovalent and divalent modes. Next, we tested each  
14  
15 binding state by coupling STM with scanning tunneling spectroscopy (STS) to monitor both the  
16  
17 exposed and buried interfaces.<sup>7,16,54</sup>  
18  
19  
20  
21

22  
23 Multimodal STM, which can simultaneously record the topographic landscape and the  
24  
25 dipolar interface, can be used to extract molecular orientations within monolayers.<sup>7,16,32,54,58-60</sup>  
26  
27 Topographic and local barrier height extrema are computed within a defined radial vector (the  
28  
29 size of one molecule) and correlations are computed *via* block-matching,<sup>61,62</sup> to associate  
30  
31 symmetric molecular apexes with dipolar extrema.<sup>7,16</sup> Here, local maxima (inverted minima)  
32  
33 within SAMs composed of **9O12** can be locally attributed to carbons at the 1- and 2- positions  
34  
35 within the cage. Conversely, local maxima within SAMs composed of **1O2** can be attributed to  
36  
37 the local dipolar offsets within the boron cage. Correlated topographic maxima to LBH extrema  
38  
39 values, shown in Rose plots (Figure 5), indicate that greater apparent protrusions in SAMs  
40  
41 composed of **1O2** have larger offsets ( $3.8 \pm 1.0 \text{ \AA}$ ) than lesser protrusions ( $2.2 \pm 0.6 \text{ \AA}$ ). In  
42  
43 SAMs composed of **9O12**, greater protrusions show slightly smaller offsets ( $1.9 \pm 0.3 \text{ \AA}$ ) in  
44  
45 comparison to lesser protrusions ( $2.6 \pm 0.6 \text{ \AA}$ ). For the small areas in the data shown, orientations  
46  
47 in each homogenous monolayer ( $283 \pm 39^\circ$  in **1O2** SAMs,  $150 \pm 33^\circ$  in **9O12** SAMs with respect  
48  
49 to the fast-scan direction, shown as horizontal, left to right, in these displayed images) suggest  
50  
51  
52  
53

1  
2  
3 charge-separation stabilization and relative dipolar alignment across each two-dimensional  
4  
5 landscape. Other orientations are found in other areas of the surfaces. These observations are  
6  
7 consistent with our binding model (monovalent and divalent modes) in each homogenous  
8  
9 monolayer. Since each binding state maintains the same nearest-neighbor spacing, the fraction of  
10  
11 sulfur bound to the Au substrate can be tailored by up to a factor of two if binding can be  
12  
13 manipulated. Motivated by the fact that each isomer is stable in both their dithiol and dithiolate  
14  
15 states,<sup>24</sup> we modify the pH to deposit either the dithiol or the dithiolate selectively. In chemical  
16  
17 lift-off lithography,<sup>29-31</sup> the amount of sulfur bound to Au may affect the amount and structure of  
18  
19 lifted-off Au from the surface. Controlling the sulfur-surface density would enable tunable  
20  
21 amounts of surface-bound Au available for patterning.<sup>63</sup>  
22  
23  
24  
25  
26

27 We tested the resulting assemblies of each carboranedithiol in both basic  
28  
29 (2:1 NaOH:carboranedithiol) and acidic conditions (1:1 HCl:carboranedithiol) with STM. Upon  
30  
31 deposition under basic conditions, majority divalent binding is achieved that is attributed to  
32  
33 deposition of the molecular dianion (dithiolate) state. Scanning tunneling microscope images  
34  
35 depict a concentration change of each phase, and show predominance of the divalent mode in  
36  
37 monolayers fabricated under basic conditions (Figure 6). Images are segmented by apparent  
38  
39 height to compute percent coverage (Figure S2). The divalent mode is dominant in each single-  
40  
41 component monolayer ( $98 \pm 2\%$  for **1O2**,  $99 \pm 1\%$  for **9O12**) under basic conditions. The small  
42  
43 fractions of the monovalent mode should appear more protruding for **1O2** but less protruding for  
44  
45 **9O12**. The possible small fractions of monovalent species after deposition from basic solution  
46  
47 may be difficult to distinguish from defects and the monolayers, in any case, are within  
48  
49 experimental error of being completely divalent.  
50  
51  
52  
53

1  
2  
3 We also performed deposition experiments in acidic conditions and measured the  
4 resulting monolayers. Saturating carboranedithiol solutions with excess protons, prior to  
5 deposition, enables somewhat higher concentrations of monovalent (thiol/thiolate) molecules, in  
6 comparison to their counterparts deposited from neutral solutions. Figure 7 depicts the  
7 topographic environment after acidic deposition, where an increase in (greater apparent  
8 protrusions) in SAMs composed of **1O2** indicate higher concentrations ( $31 \pm 3\%$ ) of monovalent  
9 (thiol/thiolate) species; SAMs composed of **9O12** already show an almost total monovalent  
10 mode (lesser protrusions) at neutral pH and hence do not show any change for a proton-rich  
11 deposition environment ( $98 \pm 1\%$ ). In summary, SAMs composed of divalent **1O2** or **9O12**  
12 (basic conditions) enable high dithiolate surface attachment, where SAMs composed of  
13 monovalent **9O12** (neutral or acidic conditions) permit low sulfur-surface attachment simply due  
14 to the controllable binding within structurally equivalent isomeric monolayers.  
15  
16  
17  
18  
19  
20  
21  
22  
23  
24  
25  
26  
27  
28  
29  
30  
31

32 In order to monitor the results of SAM formation in each environment at the ensemble  
33 scale and to complement the STM measurements, we used both X-ray photoelectron  
34 spectroscopy (XPS) and Fourier transform infrared (FTIR) spectroscopy. All measured XPS and  
35 FTIR results, and modeled values are detailed in Table 1 and Table S3, using the sulfur and  
36 similar B-H vibrational spectra under all conditions also measured with STM. Characteristic  
37 orbital energy peaks of each atomic species within the monolayer can be measured with XPS.  
38 Our results are consistent with prior XPS measurements in both monolayers deposited at neutral  
39 pH, where S 2p orbital peaks show shifts similar to previously reported values.<sup>21</sup> To test  
40 monolayer integrity, we also measured each monolayer after pH manipulation (Figures S4 and  
41 S5). Values reported for XPS not only show the retention of S 2p shifts, but also confirm the lack  
42  
43  
44  
45  
46  
47  
48  
49  
50  
51  
52  
53

1  
2  
3 of any measured  $\text{Cl}^-$  or  $\text{Na}^+$  within each monolayer after acid or base treatment. Using FTIR, we  
4 specifically tracked the B-H vibrational stretch, at  $\sim 2600 \text{ cm}^{-1}$ , which is characteristic for  
5 carboranes.<sup>19,64</sup> Measured SAMs composed of **1O2** show similar vibrational features under all  
6 conditions; however, SAMs composed of **9O12** reveal significant intensity decreases of the peak  
7 centered at  $2593 \text{ cm}^{-1}$  and loss of the peak at  $2559 \text{ cm}^{-1}$  (Figures S6 and S7), which are attributed  
8 to a change from majority monovalent to majority divalent binding in SAMs composed of **9O12**  
9 after deposition in base. Each experiment is repeated ( $n > 3$ ) to track functional control at both  
10 the local and ensemble scales. Vibrational peaks were also modeled in the gas phase using  
11 density functional theory. We attribute measured peaks in SAMs composed of **1O2** to  
12 complicated collective modes of B-H stretching vibrations that involve significant contributions  
13 from all the boron vertices. In the observed doublet, the peak at higher frequency is composed of  
14 modes dominated by stretches of B-H vertices 3, 6, and 4, 5, 7, and 11, while the modes of the  
15 lower frequency peak include predominantly the stretches of BH 8, 9, 10, and 12. In SAMs  
16 composed of **9O12**, a triplet is measured with FTIR that is also modeled (Table S3), with the  
17 calculated collective B-H stretching modes differentiated by much stronger dominance of  
18 individual vertices or their small groups. The peaks centered at  $\sim 2559 \text{ cm}^{-1}$  belong to the  
19 stretching modes with major contribution from vertices 8 and 10, peaks at  $2595 \text{ cm}^{-1}$  are  
20 dominated by stretches at vertices 4, 5, 7, and 11, and peaks at  $2633 \text{ cm}^{-1}$  are formed by the  
21 modes involving predominantly vertices 3 and 6. Frequency calculations for the gold salts of  
22 both **1O2** and **9O12** show relative attenuation of the infrared absorption features connected with  
23 the B-H stretching modes with the major contribution from the vertices close to the S atoms upon  
24 binding the sulfur atom to gold. Especially in the **9O12** layer, the intensity decrease at  
25  
26  
27  
28  
29  
30  
31  
32  
33  
34  
35  
36  
37  
38  
39  
40  
41  
42  
43  
44  
45  
46  
47  
48  
49  
50  
51  
52  
53



1  
2  
3 ~2595 cm<sup>-1</sup> and peak loss at 2595 cm<sup>-1</sup> under basic conditions are consistent with our  
4  
5 assignments and computational results. The loss of infrared absorption intensity of the stretching  
6  
7 modes dominated by the groups of 4, 5, 7, 11 and 8, 10 B-H vertices is attributed to the effect of  
8  
9 lateral intermolecular interactions.  
10

11  
12  
13 Binding configurations are further modeled on Au surfaces with all possible high-  
14  
15 symmetry binding sites on the Au{111} surface: face-centered cubic three-fold hollow sites,  
16  
17 hexagonally close-packed three-fold hollow sites, bridge sites, and atop sites. The most favorable  
18  
19 binding modalities are presented in Table 2, where the most stable **1O2** and **9O12** species are  
20  
21 presented schematically in Figures S8 and S9. Both monovalent and divalent binding modes, for  
22  
23 **1O2** and **9O12**, are energetically favorable.  
24  
25  
26  
27

28 We use both STM and STS to test the local valency within monolayers of  
29  
30 carboranedithiols on Au{111} after control *via* pH. This control is monitored by apparent height  
31  
32 in STM, dipole offsets in simultaneous STM topography and LBH measurements, infrared  
33  
34 spectroscopy, and X-ray photoelectron spectroscopy, and is supported and understood with  
35  
36 complementary density functional calculations.  
37  
38  
39  
40

## 41 **Conclusions and Prospects**

42  
43

44 We have controlled the valency of binding within SAMs composed of different  
45  
46 carboranedithiol isomers. These monolayers retain their two-dimensional lattice structures,  
47  
48 independent of their binding configuration. With this level of control, we are able to dictate  
49  
50 surface-atom-molecule stoichiometry with simple acid-base chemistry. We anticipate using these  
51  
52  
53

1  
2  
3 and related systems to explore the effects of valency on surface patterning<sup>29-31,35,36,63</sup> and  
4 dynamics.<sup>65,66</sup> A further step would be driving dynamics by chemistry, electric field,  
5 electrochemical potential, light, or other stimuli.<sup>33,42-46,67-71</sup> Systems such as these with  
6 significant chemical changes could play key roles in developing the ability to control motion at  
7 the nanoscale both for individual molecules and with coordination across assemblies.<sup>33,44,68,70</sup>  
8  
9  
10  
11  
12  
13  
14  
15

16           Creating monolayers with switchable substrate-molecule valency and bond strengths  
17 while preserving lattice constants enables exploration of this important interface and adds to the  
18 repertoire of controllable interactions at surface-molecule, molecule-molecule, and molecule-  
19 environment interfaces. By simply varying the head group, molecular backbone, and/or the tail  
20 group, extraordinary control is attainable.<sup>1-3,6,8,13</sup> Rigid cage molecules, especially  
21 carboranethiols, exhibit advantageous properties and provide test beds for independently  
22 exploring aspects of self-assembly, such as dipole interactions, molecular orientation, electron  
23 transfer, surface polarity, and now valency.<sup>3,13,15-17,31,72</sup> Here, bifunctional carboranedithiols  
24 assemble into well-ordered monolayers on Au surfaces with two distinct binding modes that are  
25 confirmed by STM, STS, FTIR, XPS, and DFT. This control is also expected to be of specific  
26 use in chemical patterning, where the binding of molecules to substrates and stoichiometry of  
27 molecule-to-surface bonds are both critical.<sup>31</sup>  
28  
29  
30  
31  
32  
33  
34  
35  
36  
37  
38  
39  
40  
41  
42  
43  
44  
45  
46  
47  
48  
49  
50  
51  
52  
53

## Materials and Methods

### *Monolayer Preparation*

The chemicals **1O2** and **9O12** were synthesized and characterized in accordance with previously published methods.<sup>21,24</sup> Ethanol was used as received (Sigma-Aldrich, St. Louis, MO). The Au{111}/mica substrates (Agilent Technology, Tempe, AZ) were hydrogen-flame annealed prior to SAM formation with 10 passes at a rate of 0.4 Hz. Both unmodified SAMs were prepared by immersion into 1 mM ethanolic solutions and held at room temperature for approximately 24 h. Short deposition times (10 min), in acidic or basic solutions, were employed to decrease the possibility of molecular degradation. After deposition, each sample was rinsed thoroughly with neat ethanol and dried under a stream of ultrahigh purity argon for at least three cycles.

Since carboranes are known to degrade upon exposure to concentrated base,<sup>73</sup> we use dilute concentrations of acid and base to prevent side reactions. Hydrochloric acid (12 M) and NaOH pellets were used as received (Sigma-Aldrich, St. Louis, MO). Acidic solutions were prepared by mixing 0.5 mL of 2 mM HCl in EtOH and 0.5 mL of 2 mM **1O2** or **9O12** in EtOH in a gasketed v-vial. Basic solutions were prepared by mixing 0.5 mL of 4 mM NaOH in EtOH and 0.5 mL of 2 mM **1O2** or **9O12** in EtOH. Monolayers were prepared by immersing flame-annealed Au{111}/mica substrates into modified solutions for 1 h. Larger ratios of both acid (2:1) and base (4:1) were tested, however, no differences were found.

### *Scanning Tunneling Microscopy*

1  
2  
3 All STM measurements were performed with either a custom-built Besocke-style  
4 scanning tunneling microscope under ambient conditions or a custom-built Besocke-style  
5 scanning tunneling microscope held at cryogenic (4 K) and extreme high vacuum ( $<10^{-12}$  torr)  
6 conditions.<sup>74,75</sup> Samples were held at a fixed bias ( $V_{\text{sample}} = -0.5$  V) and both topographic and  
7 LBH modalities were measured in a constant current fashion ( $I_t = 15$  pA). The tunneling gap  
8 distance was modulated above the microscope feedback loop ( $\sim 3$  kHz) with a sinusoidal  
9 amplitude ( $dz \sim 0.1$  Å) and  $dI/dz$  was measured with a lock-in technique (Stanford Research  
10 Systems SR850 DSP, Sunnyvale, CA).<sup>7,57</sup> The well-known lattice of atomic Au{111}, held at  
11 4 K, was measured and used to calibrate all low temperature images, and the known lattice  
12 within SAMs of 1-dodecanethiolate were used to calibrate all images obtained at room  
13 temperature.  
14  
15  
16  
17  
18  
19  
20  
21  
22  
23  
24  
25  
26  
27  
28

### 29 *Image Analyses*

30  
31  
32 All STM images were processed with automated routines developed in MATLAB  
33 (Mathworks, Natick, MA) to remove high-frequency noise and intensity spikes that may impair  
34 reliable interpretation.<sup>7</sup> Local maxima (minima) for both topography and local barrier height  
35 images were chosen as the highest (lowest) intensity pixel within a defined radial vector (the size  
36 of one molecule). Dipole offsets were computed using a block-matching approach,<sup>16,61,62</sup> where  
37 topographic image patches (size of one molecule) were correlated against larger local barrier  
38 height image patches (size of the nearest-neighbor spacing) to obtain a set of points ( $p$  and  $q$ ) that  
39 were referenced and plotted. Correlated values (shown in Figure 5) were compared against  
40 connecting all points within a defined pixel radius, as a function of size, where correlation  
41  
42  
43  
44  
45  
46  
47  
48  
49  
50  
51  
52  
53

1  
2  
3 yielded the least artifacts (Figures S8 and S9). Gray scale threshold values were chosen based on  
4  
5 apparent height differences to produce binary image highlights, which were further used to  
6  
7 obtain percent coverages.  
8  
9

### 10 11 *Infrared Spectroscopy*

12  
13  
14 All infrared spectra were collected with a Nicolet 6700 FTIR spectrometer (Thermo  
15  
16 Electron Corp., Waltam, MA) that was equipped with a mercury-cadmium-telluride detector,  
17  
18 held at liquid nitrogen temperatures, and a Seagull variable-angle reflection accessory (Harrick  
19  
20 Scientific, Inc., Ossining, NY). Water and carbon dioxide were removed from the spectrometer  
21  
22 by an FTIR purge gas generator (Parker-Balston, Cleveland, OH). A grazing incidence reflection  
23  
24 angle ( $82^\circ$  with respect to the surface normal) with *p*-polarized light, a mirror speed of 1.27 cm/s,  
25  
26 and a resolution of  $2\text{ cm}^{-1}$ . Spectra were averaged over 5120 scans and normalized against  
27  
28 spectra of perdeuterated *n*-dodecanethiolate monolayers on Au{111}.  
29  
30  
31  
32

### 33 34 *X-Ray Photoelectron Spectroscopy*

35  
36  
37 All XPS spectra were collected with an AXIS Ultra DLD instrument (Kratos Analytical  
38  
39 Inc., Chestnut Ridge, NY). A monochromatic Al  $K_\alpha$  X-ray source (20 mA, 15 kV) with a 200  $\mu\text{m}$   
40  
41 circular spot size that was held at ultrahigh vacuum ( $10^{-9}$  torr) were used for all measurements.  
42  
43 Spectra were acquired at a pass energy of 160 eV for survey spectra and 20 eV for high  
44  
45 resolution spectra of S 2p, C 1s, B 1s, and Au 4f regions that used a 200 ms dwell time. Different  
46  
47 numbers of scans were carried out depending on the amount required for high-resolution spectra,  
48  
49 which ranged from 20 scans for C 1s to 75 scans for S 2p. Binding energies were calibrated to  
50  
51  
52  
53

1  
2  
3 the Au 4f peak at 83.98 eV.<sup>76</sup> Spectra were fit using CasaXPS software with Gaussian-  
4 Lorentzian lineshapes after Shirley background subtraction. Sulfur regions were fitted by a  
5  
6 doublet structure with a 1.18 eV spin-orbit splitting and a defined intensity ratio (2p<sub>3/2</sub>:2p<sub>1/2</sub>, 2:1).  
7  
8  
9

### 10 11 *Computational Modeling*

12  
13  
14 Density functional theory calculations were performed to understand the molecular  
15 chemisorption modes and their relation with the STM imaging. Geometry optimizations were  
16 performed with the plane-wave periodic DFT VASP program.<sup>77-80</sup> Exchange and correlation  
17 effects were described within the generalized gradient approximation (GGA), using the Perdew-  
18 Burke-Ernzerhof (PBE) functional<sup>81</sup> and electron-ion interactions are treated with the projector  
19 augmented wave approach.<sup>82</sup> In order to describe the dispersion interactions, the empirically  
20 constructed DFT-D3 method was used.<sup>83</sup> The calculations were done in a spin-unrestricted  
21 fashion when applicable. The gold slab was modeled as a ( $\sqrt{7}\times\sqrt{7}$ )R19.12° supercell, with four  
22 layers along z. The bottom two layers were fixed during the optimization. The calculated lattice  
23 constant for Au was 2.95 Å, in good agreement with the experiment.  
24  
25  
26  
27  
28  
29  
30  
31  
32  
33  
34  
35  
36  
37

38 To avoid spurious interactions between images in the z-direction, a vacuum gap of 10 Å  
39 was inserted between the highest atom of the carboranedithiolate molecules, and the repeated  
40 image of the slab's bottom layer. The cutoff energy for the plane-wave basis set was chosen to be  
41 400 eV. A 5×5×1 Monkhorst-Pack k-point grid allowed for the numerical solution of  
42 Hamiltonian and overlap matrix elements. For the STM images and the charge density plots a  
43 denser k point grid (11×11×1) was used.  
44  
45  
46  
47  
48  
49  
50  
51  
52  
53

1  
2  
3 The STM images were simulated using the Tersoff-Hamann method<sup>47</sup> using VASP.  
4  
5  
6  
7

8 Natural bond order (NBO1.1)<sup>84</sup> analyses of the molecules on the support were performed.  
9  
10 The periodic version of NBO also requires the wave function to be represented in an atom-  
11 centered basis, therefore we projected the plane-wave solution onto the Def2-TZVP<sup>85,86</sup>  
12 Gaussian-type orbital basis set.  
13  
14  
15  
16  
17  
18  
19  
20  
21  
22  
23  
24  
25  
26  
27  
28  
29  
30  
31  
32  
33  
34  
35  
36  
37  
38  
39  
40  
41  
42  
43  
44  
45  
46  
47  
48  
49  
50  
51  
52  
53

## FIGURES

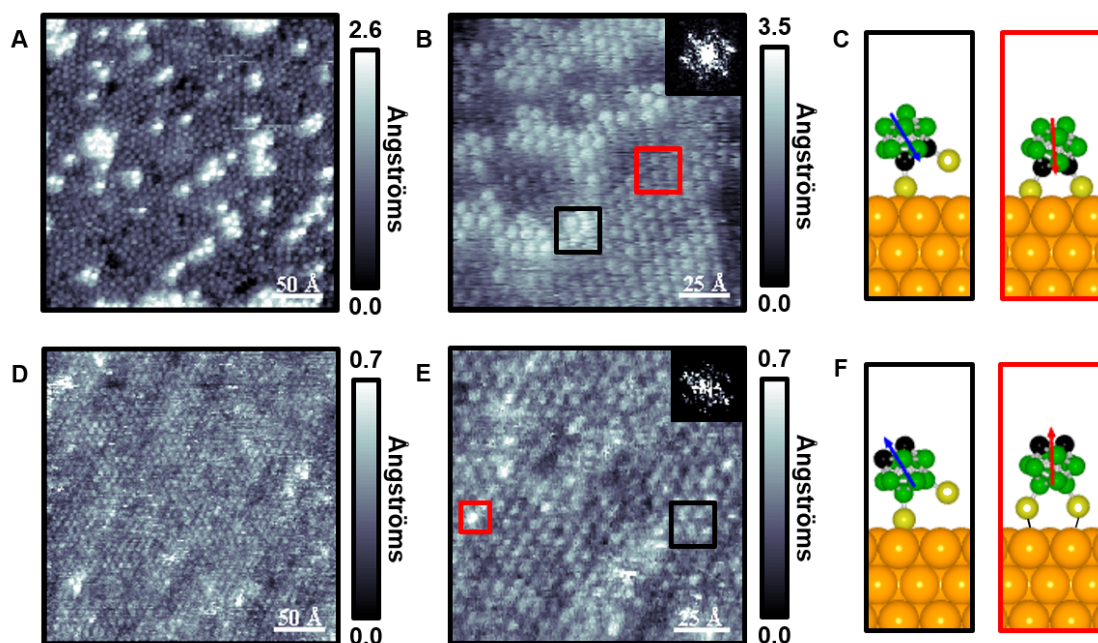


**Figure 1.** Scanning tunneling microscope images of (A,B) 1,2-(HS)<sub>2</sub>-1,2-C<sub>2</sub>B<sub>10</sub>H<sub>10</sub> (**1O2**) on Au{111}/mica at two different resolutions ( $V_{\text{sample}} = -0.1$  V,  $I_{\text{tunneling}} = 100$  pA,  $T = 298$  K). Insets depict fast Fourier transforms (FFTs) that indicate hexagonally close-packed arrangements with nearest-neighbor spacings of  $7.6 \pm 0.5$  Å. Two distinct binding states are highlighted in red and black. (C) Binding modes are shown schematically, where **1O2** assembles into both monovalent (black box) and divalent (red box) modes. (D,E) Scanning tunneling microscope images ( $V_{\text{sample}} = -0.1$  V,  $I_{\text{tunneling}} = 100$  pA,  $T = 298$  K) of 9,12-(HS)<sub>2</sub>-1,2-C<sub>2</sub>B<sub>10</sub>H<sub>10</sub> (**9O12**) on Au{111}/mica at different resolutions. The inset depicts a FFT showing a hexagonally close-packed arrangement with the same spacing as **1O2**. The two binding states are highlighted schematically in red and black boxes. (F) Binding modes for **9O12** are depicted schematically, where both monovalent (black box) and divalent (red box) modes are present.



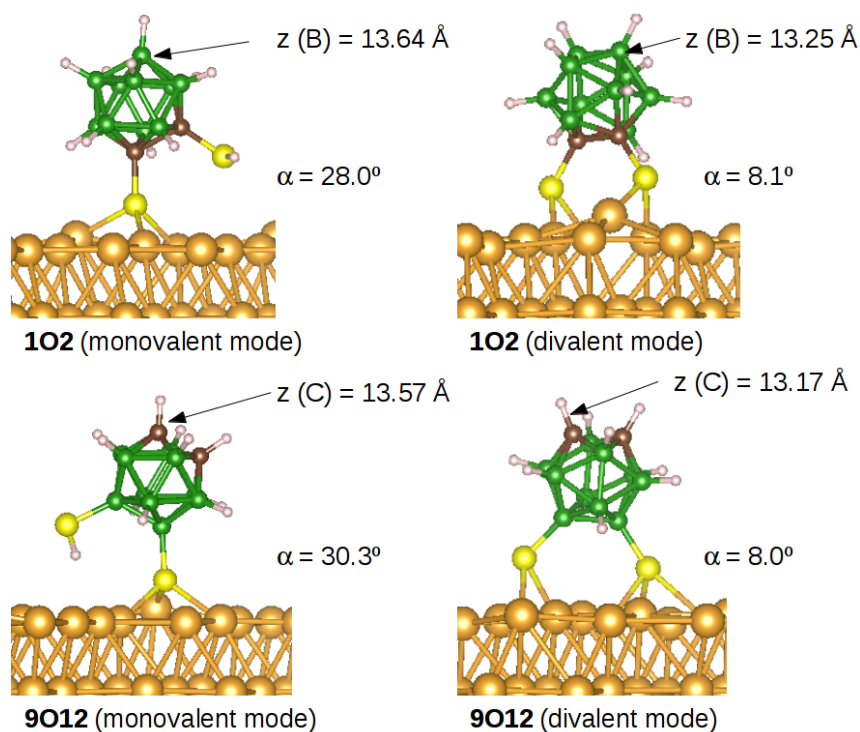


**Figure 2.** Preferred structures/binding sites for **1O<sub>2</sub>** and **9O<sub>2</sub>** in their respective monovalent and divalent binding modes. The z coordinate of the uppermost atom (without considering H atoms) and the tilt angles of the molecules with respect to the surface normal ( $\alpha$ ) are shown for each case.

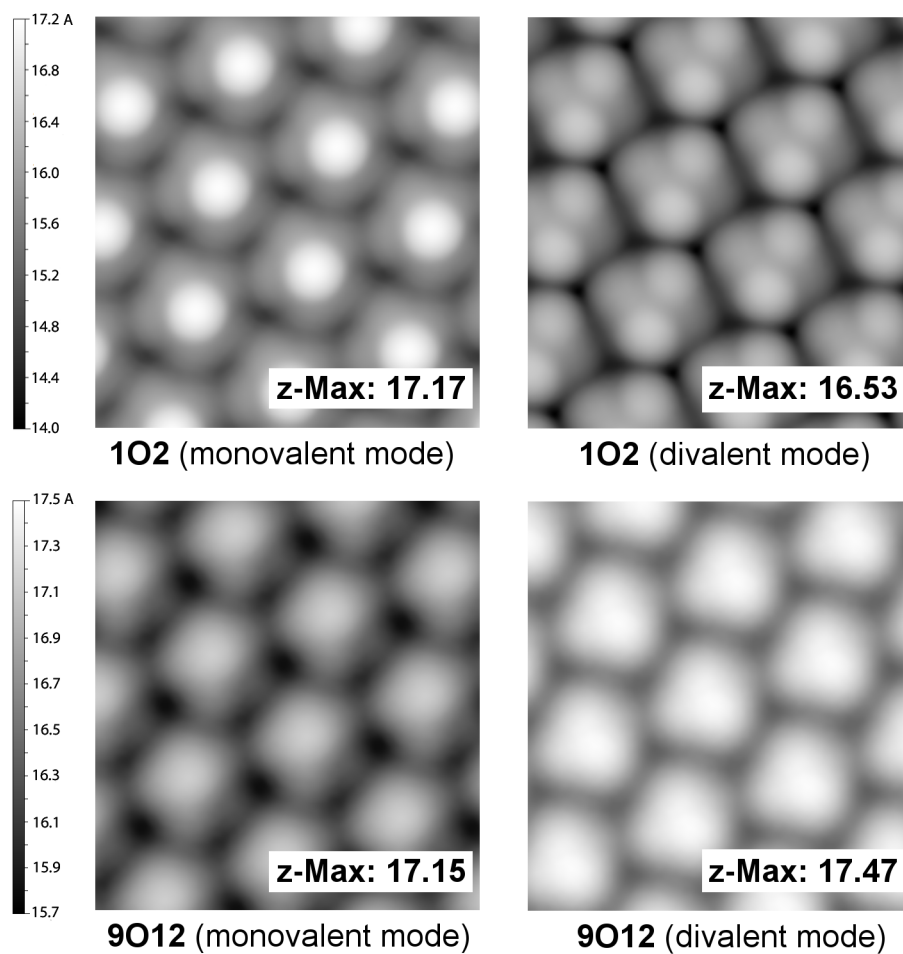
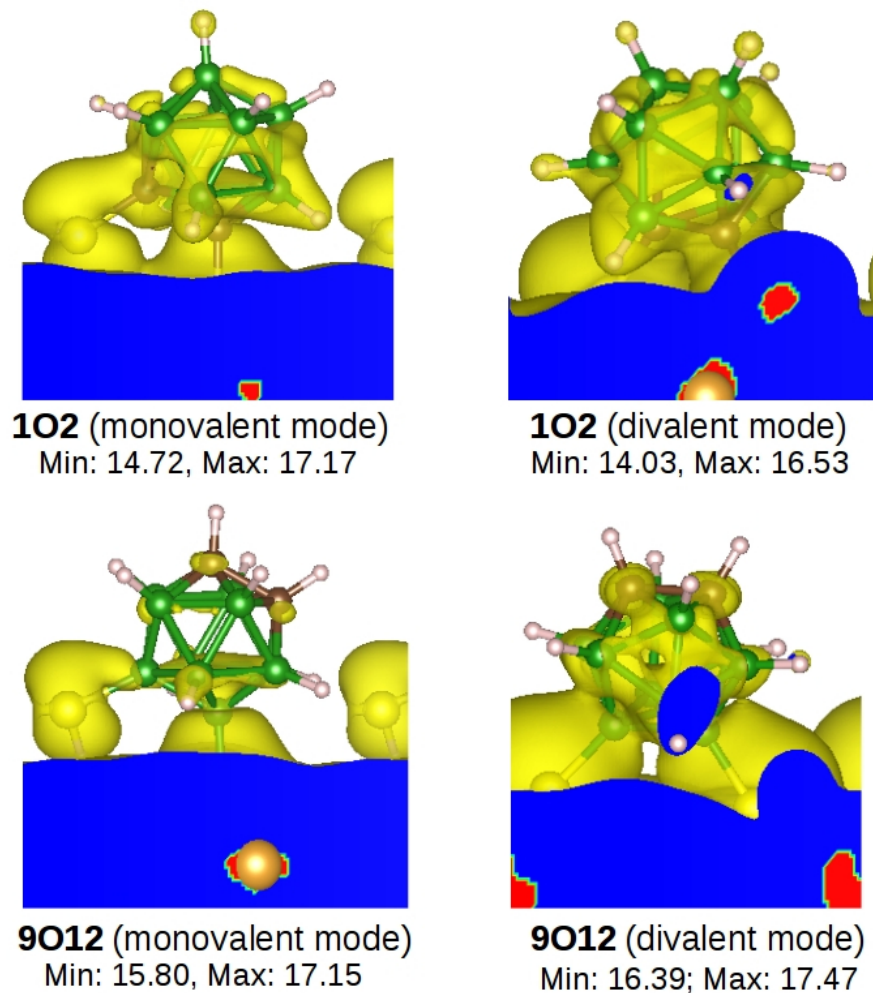


**Figure 3.** Simulated scanning tunneling microscope images for **1O2** and **9O2** in their respective monovalent and divalent binding modes, with the maximum height shown in the insets (in Å).

The  $10^{-4}$  isovalue for the charge density was used.



37 **Figure 4.** Charge density plots from the Fermi energy to  $E_f - 0.1$  eV for (top) **102** and (bottom)  
38 **9012** in their respective (left) monovalent and (right) divalent binding modes. The images are  
39 plotted with an isodensity value of 0.00002, because most of the charge density is located on the  
40 gold surface. “Min” and “Max” stand for the minimum and maximum topographic ranges (in Å),  
41  
42  
43  
44  
45  
46  
47  
48  
49  
50  
51  
52  
53  
54  
55  
56  
57  
58  
59  
60

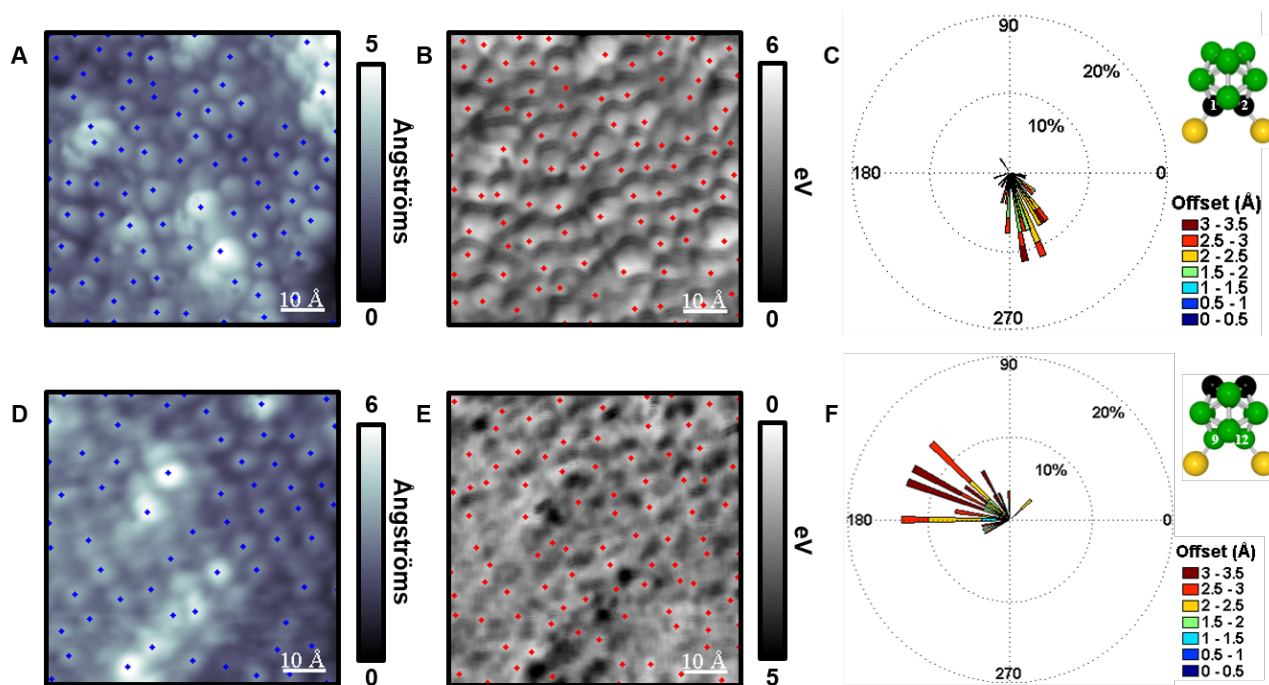


**Figure 5.** (A) Scanning tunneling microscope images, recorded at low temperature ( $V_{\text{sample}} = -0.5$  V,  $I_{\text{tunneling}} = 15$  pA,  $T = 4$  K) of 1,2-(HS)<sub>2</sub>-1,2-C<sub>2</sub>B<sub>10</sub>H<sub>10</sub> (**1O2**) on Au{111} with local maxima (blue) highlighted. (B) Simultaneously acquired local barrier height (LBH) image, with LBH maxima (red) highlighted. (C) Rose plot (depicting correlated dipole offsets) that is binned by both magnitude (0.5 Å bins) and orientation (4° bins), and a ball-and-stick model of **1O2** showing thiol positions. (D) Scanning tunneling microscope image, recorded at low temperature ( $V_{\text{sample}} = -0.5$  V,  $I_{\text{tunneling}} = 15$  pA,  $T = 4$  K) of 9,12-(HS)<sub>2</sub>-1,2-C<sub>2</sub>B<sub>10</sub>H<sub>10</sub> (**9O12**) on Au{111} with local maxima (blue) highlighted. (E) Simultaneously acquired LBH map, with inverted LBH maxima (red) highlighted. (F) Rose plot (depicting correlated dipole offsets) that is binned by both magnitude (0.5 Å bins) and orientation (4° bins), and a ball-and-stick model of **9O12**.

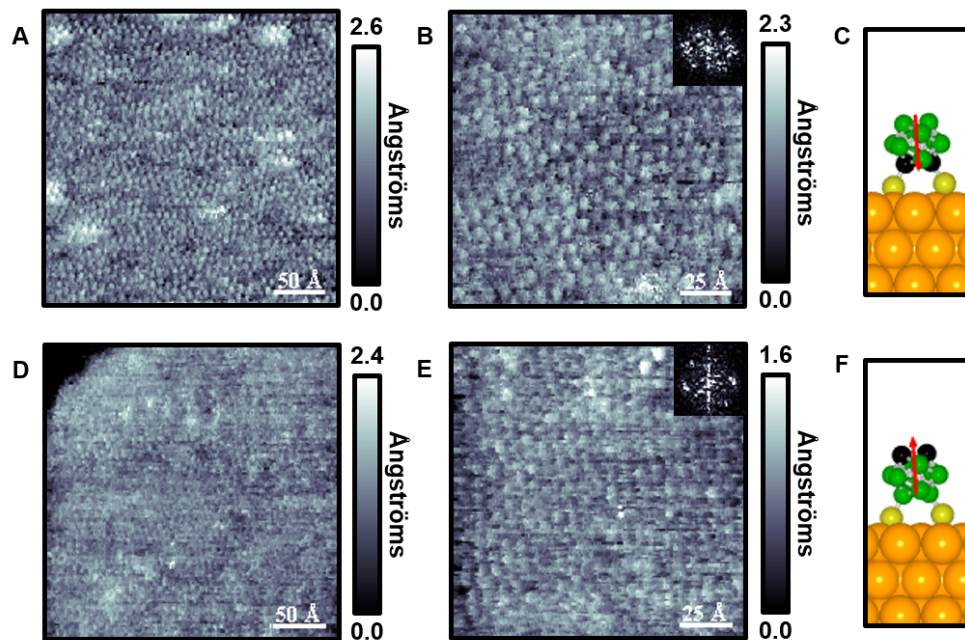


**Figure 6.** (A,B) Scanning tunneling microscope images ( $V_{\text{sample}} = -0.1$  V,  $I_{\text{tunneling}} = 100$  pA,  $T = 298$  K) of 1,2-(HS)<sub>2</sub>-1,2-C<sub>2</sub>B<sub>10</sub>H<sub>10</sub> (**1O2**) on Au{111}/mica at two different resolutions after basic deposition conditions (2:1, NaOH:**1O2**). Insets depict fast Fourier transforms (FFTs) that show hexagonally close-packed arrangements with the same nearest-neighbor spacings as in Figure 1. (C) A majority of the **1O2** molecules have divalent surface attachment, depicted schematically. (D,E) Scanning tunneling topographs ( $V_{\text{sample}} = -0.1$  V,  $I_{\text{tunneling}} = 100$  pA,  $T = 298$  K) of 9,12-(HS)<sub>2</sub>-1,2-C<sub>2</sub>B<sub>10</sub>H<sub>10</sub> (**9O12**) on Au{111}/mica at different resolutions after basic deposition (2:1, NaOH:**9O12**). Inset depicts a FFT showing the same arrangement and spacing as **1O2**. (F) A divalently bound **9O12** molecule is shown schematically.

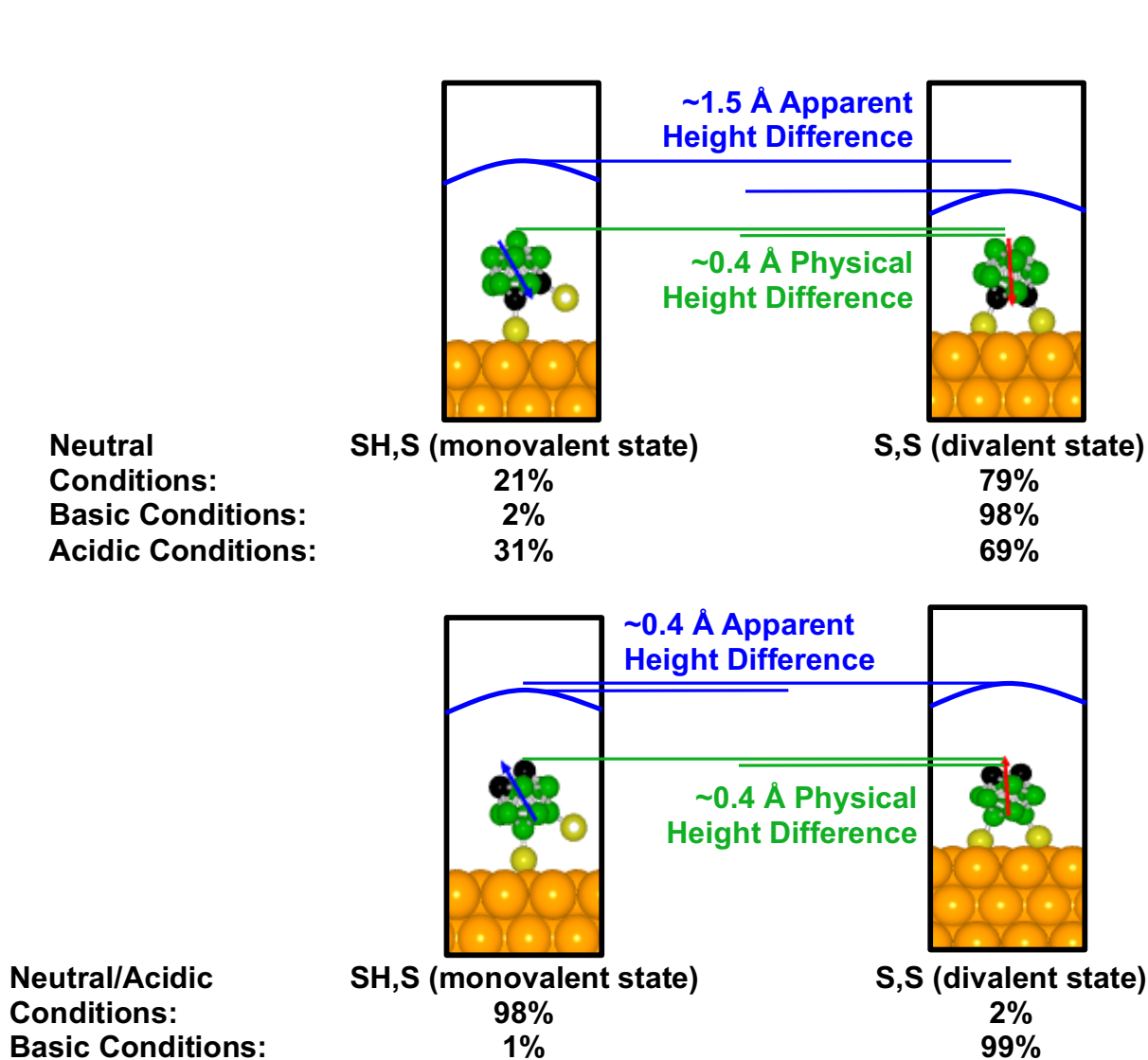


**Figure 7.** Binding assignments measured by scanning tunneling microscopy and scanning tunneling spectroscopy (STS). (Top) Self-assembled monolayers composed of 1,2-(HS)<sub>2</sub>-1,2-C<sub>2</sub>B<sub>10</sub>H<sub>10</sub> (**1O2**) form into (left) a thiol/thiolate state (monovalent form) and (right) a dithiolate state (divalent form) that differ in apparent height in scanning tunneling microscope images. (Bottom) Monolayers composed of 9,12-(HS)<sub>2</sub>-1,2-C<sub>2</sub>B<sub>10</sub>H<sub>10</sub> (**9O12**) form into (left) an adsorbed monothiol/monothiolate (monovalent) state, under acidic and neutral conditions and (right) a dithiolate (divalent) state that differ in measured apparent height, as shown for the conditions

1  
2  
3 shown in figure 1. Upon deposition under basic conditions, majority dithiolate binding is  
4  
5 observed for both isomers, as determined by STM imaging.  
6  
7  
8  
9  
10  
11  
12  
13  
14  
15  
16  
17  
18  
19  
20  
21  
22  
23  
24  
25  
26  
27  
28  
29  
30  
31  
32  
33  
34  
35  
36  
37  
38  
39  
40  
41  
42  
43  
44  
45  
46  
47  
48  
49  
50  
51  
52  
53

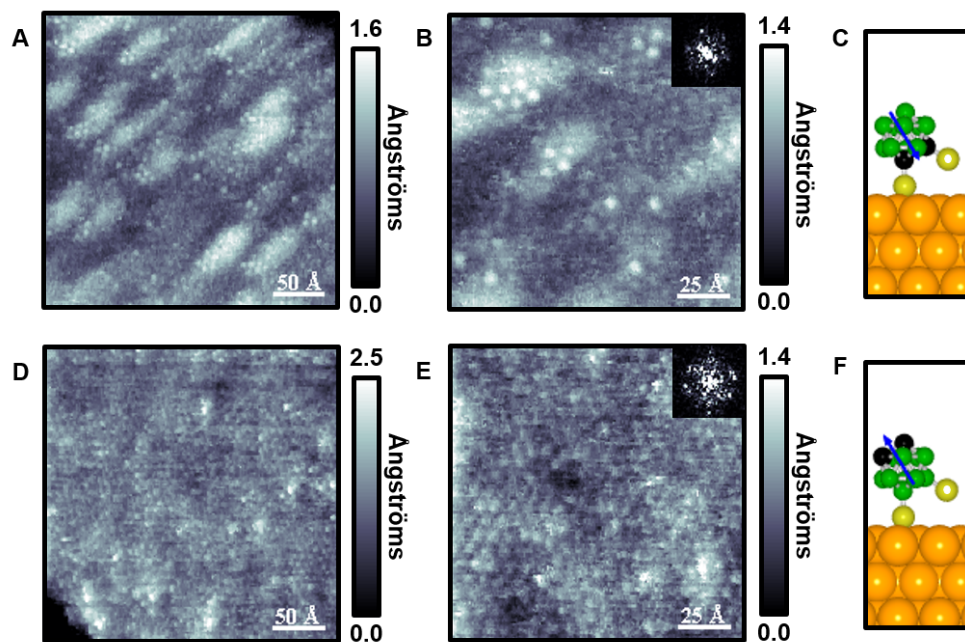


**Figure 8.** (A,B) Scanning tunneling microscope images ( $V_{\text{sample}} = -0.1$  V,  $I_{\text{tunneling}} = 100$  pA,  $T = 298$  K) of 1,2-(HS)<sub>2</sub>-1,2-C<sub>2</sub>B<sub>10</sub>H<sub>10</sub> (**1O12**) on Au{111}/mica at two different resolutions under acidic deposition conditions (1:1, HCl:**1O12**). Inset depicts a fast Fourier transform (FFT) that shows a hexagonally close-packed arrangement with the same nearest-neighbor spacings measured in both basic and neutral conditions. (C) A minority push to the monovalent binding is achieved and depicted schematically. (D,E) Scanning tunneling topographs ( $V_{\text{sample}} = -0.1$  V,  $I_{\text{tunneling}} = 100$  pA,  $T = 298$  K) of 9,12-(HS)<sub>2</sub>-1,2-C<sub>2</sub>B<sub>10</sub>H<sub>10</sub> (**9O12**) on Au{111}/mica at different resolutions after acidic deposition (1:1, HCl:**9O12**). Inset depicts a FFT showing the same arrangement and spacing as in neutral conditions. (F) As monolayers composed of **9O12** are already predominately monovalent, no change is measured, in comparison to neutral deposition conditions, for this system that is depicted schematically.



	<b>1O2 n</b>	<b>9O12 n</b>	<b>1O2 b</b>	<b>9O12 b</b>	<b>1O2 a</b>	<b>9O12 a</b>
Au 4f	84.0 eV	84.0 eV	84.0 eV	84.0 eV	84.0 eV	84.0 eV
B 1s	189.0 eV	189.0 eV	189.0 eV	189.0 eV	189.0 eV	189.0 eV
S 2p	162.2 eV	161.7 eV	162.2 eV	161.7 eV	162.2 eV	161.7 eV
C 1s	285.0 eV	285.0 eV	285.0 eV	285.0 eV	285.0 eV	285.0 eV
Na 1s	-	-	-	-	-	-
Cl 2p	-	-	-	-	-	-
B-H (FTIR)	2589 cm <sup>-1</sup>	2559 cm <sup>-1</sup>	2584 cm <sup>-1</sup>	2593 cm <sup>-1</sup>	2600 cm <sup>-1</sup>	2564 cm <sup>-1</sup>
	2598 cm <sup>-1</sup>	2595 cm <sup>-1</sup>	2596 cm <sup>-1</sup>	2627 cm <sup>-1</sup>	2591 cm <sup>-1</sup>	2598 cm <sup>-1</sup>
		2633 cm <sup>-1</sup>				2630 cm <sup>-1</sup>

**Table 1.** X-ray photoelectron spectroscopy energy shifts and Fourier transform spectroscopy frequency values in the B-H region (row). Columns are titled with 1,2-(HS)<sub>2</sub>-1,2-C<sub>2</sub>B<sub>10</sub>H<sub>10</sub> (**1O2**) or 9,12-(HS)<sub>2</sub>-1,2-C<sub>2</sub>B<sub>10</sub>H<sub>10</sub> (**9O12**) and labeled with neutral (n), basic (b), or acidic (a) deposition conditions.

## ASSOCIATED CONTENT

**Supporting Information.** Figures that depict image binaries used for coverage calculations, X-ray photoelectron spectroscopy, Fourier transform infrared spectroscopy, image correlation, tabulated frequency calculation results, and calculated atomic coordinates. This material is available free of charge *via* the Internet at <http://pubs.acs.org>.

## AUTHOR INFORMATION

Corresponding authors

\*[psw@cnsi.ucla.edu](mailto:psw@cnsi.ucla.edu) (P. S. W.)

\*[tbase@iic.cas.cz](mailto:tbase@iic.cas.cz) (T. B.)

\*[ana@chem.ucla.edu](mailto:ana@chem.ucla.edu) (A. A.)

## ORCID

Dominic P. Goronzy: 0000-0003-2856-4732

Andrew C. Serino: 0000-0003-2767-1026

Elisa Jimenez-Izal: 0000-0003-1127-2100

Jacqueline M. Deirmenjian: 0000-0003-0562-2151

Jan Macháček: 0000-0003-4723-0789

1  
2  
3 Philippe Sautet: 0000-0002-8444-3348  
4

5 Anastassia N. Alexandrova: 0000-0002-3003-1911  
6

7 Paul S. Weiss: 0000-0001-5527-6248  
8  
9

## 10 11 **ACKNOWLEDGMENTS** 12

13 We thank the DoE (grant #DE-SC-0005025) for support of the instrumentation and methods  
14 developed and applied here and the W. M. Keck Foundation for support of the development of  
15 the image analysis methods used. ANA thanks NSF CAREER Award CHE1351968. Financial  
16 support for E. J. I. comes from a Postdoctoral Fellowship of the Government of the Basque  
17 Country and NSF-CAREER Award CHE-1351968 to A.N.A. We also acknowledge the Extreme  
18 Science and Engineering Discovery Environment (XSEDE), which is supported by National  
19 Science Foundation grant number ACI-1548562, and the UCLA-IDRE cluster. This research is  
20 part of the Blue Waters sustained-petascale computing project, which is supported by the  
21 National Science Foundation (awards OCI-0725070 and ACI-1238993) and the state of Illinois.  
22 Blue Waters is a joint effort of the University of Illinois at Urbana-Champaign and its National  
23 Center for Supercomputing Applications. We gratefully thank Dr. Andrew I. Guttentag, Dr.  
24 James N. Hohman, Prof. Alex Spokoyny, and Logan Stewart for their support and helpful  
25 discussions, and Baz Luhrmann and Henri de Toulouse-Lautrec for inspiration.  
26  
27  
28  
29  
30  
31  
32  
33  
34  
35  
36  
37  
38  
39  
40  
41  
42  
43  
44  
45  
46  
47  
48  
49  
50  
51  
52  
53

**REFERENCES**

1. Love, J. C.; Estroff, L. A.; Kriebel, J. K.; Nuzzo, R. G.; Whitesides, G. M. Self-Assembled Monolayers of Thiolates on Metals as a Form of Nanotechnology. *Chem. Rev.* **2005**, *105*, 1103–1170.
2. Weiss, P. S. Functional Molecules and Assemblies in Controlled Environments: Formation and Measurements. *Acc. Chem. Res.* **2008**, *41*, 1772–1781.
3. Claridge, S. A.; Liao, W. S.; Thomas, J. C.; Zhao, Y.; Cao, H. H.; Cheunkar, S.; Serino, A. C.; Andrews, A. M.; Weiss, P. S. From the Bottom Up: Dimensional Control and Characterization in Molecular Monolayers. *Chem. Soc. Rev.* **2013**, *42*, 2725–2745.
4. Ulman, A. Formation and Structure of Self-Assembled Monolayers. *Chem. Rev.* **1996**, *96*, 1533–1554.
5. Poirier, G. E. Characterization of Organosulfur Molecular Monolayers on Au(111) using Scanning Tunneling Microscopy. *Chem. Rev.* **1997**, *97*, 1117–1128.
6. Smith, R. K.; Lewis, P. A.; Weiss, P. S. Patterning Self-Assembled Monolayers. *Prog. Surf. Sci.* **2004**, *75*, 1–68.
7. Han, P.; Kurland, A. R.; Giordano, A. N.; Nanayakkara, S. U.; Blake, M. M.; Pochas, C. M.; Weiss, P. S. Heads and Tails: Simultaneous Exposed and Buried Interface Imaging of Monolayers. *ACS Nano* **2009**, *3*, 3115–3121.

- 1  
2  
3 8. Hohman, J. N.; Thomas, J. C.; Zhao, Y.; Auluck, H.; Kim, M.; Vijselaar, W.; Kommeren, S.;  
4 Terfort, A.; Weiss, P. S. Exchange Reactions between Alkanethiolates and Alkaneselenols on  
5 Au{111}. *J. Am. Chem. Soc.* **2014**, *136*, 8110–8121.  
6  
7  
8  
9  
10  
11 9. Salmeron, M.; Neubauer, G.; Folch, A.; Tomitori, M.; Ogletree, D. F.; Sautet, P. Viscoelastic  
12 and Electrical Properties of Alkylthiol Monolayers on Gold(111) Films. *Langmuir* **1993**, *9*,  
13 3600–3611.  
14  
15  
16  
17  
18  
19 10. Nuzzo, R. G.; Allara, D. L. Adsorption of Bifunctional Organic Disulfides on Gold Surfaces.  
20 *J. Am. Chem. Soc.* **1983**, *105*, 4481–4483.  
21  
22  
23  
24  
25 11. Takami, T.; Delamarche, E.; Michel, B.; Gerber, Ch.; Wolf, H.; Ringsdorf, H. Recognition of  
26 Individual Tail Groups in Self-Assembled Monolayers. *Langmuir* **1995**, *11*, 3876–3881.  
27  
28  
29  
30 12. Kim, M.; Hohman, J. N.; Cao, Y.; Houk, K. N.; Ma, H.; Jen, A. K.; Weiss, P. S. Creating  
31 Favorable Geometries for Directing Organic Photoreactions in Alkanethiolate Monolayers.  
32 *Science* **2011**, *331*, 1312–1315.  
33  
34  
35  
36  
37  
38 13. Hohman, J. N.; Claridge, S. A.; Kim, M.; Weiss, P. S. Cage Molecules for Self-Assembly.  
39 *Mater. Sci. Eng. R* **2010**, *70*, 188–208.  
40  
41  
42  
43  
44 14. Spokoyny, A. M.; Machan, C. W.; Clingerman, D. J.; Rosen, M. S.; Wiester, M. J.; Kennedy,  
45 R. D.; Stern, C. L.; Sarjeant, A. A.; Mirkin, C. A. A Coordination Chemistry Dichotomy for  
46 Icosahedral Carborane-Based Ligands. *Nat. Chem.* **2011**, *3*, 590–596.  
47  
48  
49  
50  
51  
52  
53

- 1  
2  
3 15. Kim, J.; Rim, Y. S.; Liu, Y.; Serino, A. C.; Thomas, J. C.; Chen, H.; Yang, Y.; Weiss, P. S.  
4 Interface Control in Organic Electronics Using Mixed Monolayers of Carboranethiol Isomers.  
5  
6 *Nano Lett.* **2014**, *14*, 2946–2951.  
7  
8  
9  
10  
11 16. Thomas, J. C.; Schwartz, J. J.; Hohman, J. N.; Claridge, S. A.; Auluck, H. S.; Serino, A. C.;  
12 Spokoyny, A. M.; Tran, G.; Kelly, K. F.; Mirkin, C. A.; Gilles, J.; Osher, S. J.; Weiss, P. S.  
13 Defect-Tolerant Aligned Dipoles within Two-Dimensional Plastic Lattices. *ACS Nano* **2015**, *9*,  
14 4734–4742.  
15  
16  
17  
18  
19  
20  
21 17. Thomas, J. C.; Boldog, I.; Auluck, H. S.; Bereciartua, P.; Dušek, M.; Macháček, J.; Bastl, Z.;  
22 Weiss, P. S.; Baše, T. Self-Assembled *p*-Carborane Analog of *p*-Mercaptobenzoic Acid on  
23 Au{111}. *Chem. Mater.* **2015**, *27*, 5425–5435.  
24  
25  
26  
27  
28  
29 18. Kristiansen, K.; Stock, P.; Baimpos, T.; Raman, S.; Harada, J. K.; Israelachvili, J. N.;  
30 Valtiner, M. Influence of Molecular Dipole Orientations on Long-Range Exponential Interaction  
31 Forces at Hydrophobic Contacts in Aqueous Solutions. *ACS Nano* **2014**, *8*, 10870–10877.  
32  
33  
34  
35  
36  
37 19. Hohman, J. N.; Zhang, P.; Morin, E. I.; Han, P.; Kim, M.; Kurland, A. R.; McClanahan, P.  
38 D.; Balema, V. P.; Weiss, P. S. Self-Assembly of Carboranethiol Isomers on Au{111}:  
39 Intermolecular Interactions Determined by Molecular Dipole Orientations. *ACS Nano* **2009**, *3*,  
40 527–536.  
41  
42  
43  
44  
45  
46  
47 20. Serino, A. C.; Anderson, M. E.; Saleh, L. M. A.; Dziedzic, R. M.; Mills, H.; Heidenreich, L.  
48 K.; Spokoyny, A. M.; Weiss, P. S. Work Function Control of Germanium through Carborane-  
49 Carboxylic Acid Surface Passivation. *ACS Appl. Mater. Interfaces* **2017**, *9*, 34592–34596.  
50  
51  
52  
53  
54

- 1  
2  
3 21. Baše, T.; Bastl, Z.; Plzák, Z.; Grygar, T.; Plešek, J.; Carr, M.; Malina, V.; Šubrt, J.; Boháček,  
4 J.; Večerníková, E.; Kříž, O. Carboranethiol-Modified Gold Surfaces. A Study and Comparison  
5 of Modified Cluster and Flat Surfaces. *Langmuir* **2005**, *21*, 7776–7785.  
6  
7  
8  
9  
10  
11 22. Baše, T.; Bastl, Z.; Šlouf, M.; Klementová, M.; Šubrt, J.; Vetushka, A.; Ledinský, M.; Fejfar,  
12 A.; Macháček, J.; Carr, M. J.; Londesborough, M. G. S. Gold Micrometer Crystals Modified  
13 with Carboranethiol Derivatives. *J. Phys. Chem. C* **2008**, *112*, 14446–14455.  
14  
15  
16  
17  
18  
19 23. Baše, T.; Bastl, Z.; Havránek, V.; Lang, K.; Bould, J.; Londesborough, M. G. S.; Macháček,  
20 J.; Plešek, J. Carborane-Thiol-Silver Interactions. A Comparative Study of the Molecular  
21 Protection of Silver Surfaces. *Surf. Coat. Tech.* **2010**, *204*, 2639–2646.  
22  
23  
24  
25  
26  
27 24. Lübben, J. F.; Baše, T.; Rupper, P.; Künniger, T.; Macháček, J.; Guimond, S. Tuning the  
28 Surface Potential of Ag Surfaces by Chemisorption of Oppositely-Oriented Thiolated Carborane  
29 Dipoles. *J. Colloid Interface Sci.* **2011**, *354*, 168–174.  
30  
31  
32  
33  
34  
35 25. Langecker, J.; Fejfarová, K.; Dušek, M.; Rentsch, D.; Baše, T. Carbon-Substituted 9,12-  
36 Dimercapto-1,2-Dicarba-*closo*-Dodecaboranes via a 9,12-Bis(Methoxy-Methylthio)-1,2-  
37 Dicarba-*closo*-Dodecaborane Precursor. *Polyhedron* **2012**, *45*, 144–151.  
38  
39  
40  
41  
42  
43 26. Baše, T.; Bastl, Z.; Havránek, V.; Macháček, J.; Langecker, J.; Malina, V. Carboranedithiols:  
44 Building Blocks for Self-Assembled Monolayers on Copper Surfaces. *Langmuir* **2012**, *28*,  
45 12518–12526.  
46  
47  
48  
49  
50  
51  
52  
53

- 1  
2  
3 27. Schwartz, J. J.; Mendoza, A. M.; Wattanatorn, N.; Zhao, Y.; Nguyen, V. T.; Spokoyny, A.  
4 M.; Mirkin, C. A.; Base, T.; Weiss, P. S. Surface Dipole Control of Liquid Crystal Alignment. *J.*  
5 *Am. Chem. Soc.* **2016**, *49*, 5957–5967.  
6  
7  
8  
9  
10  
11 28. Nuzzo, R. G.; Dubois, L. H.; Allara, D. L. Fundamental Studies of Microscopic Wetting on  
12 Organic-Surfaces. 1. Formation and Structural Characterization of a Self-Consistent Series of  
13 Polyfunctional Organic Monolayers. *J. Am. Chem. Soc.* **1990**, *112*, 558–569.  
14  
15  
16  
17  
18  
19 29. Liao, W. S.; Cheunkar, S.; Cao, H. H.; Bednar, H. R.; Weiss, P. S.; Andrews, A. M.  
20 Subtractive Patterning *via* Chemical Lift-off Lithography. *Science* **2012**, *337*, 1517–1521.  
21  
22  
23  
24 30. Kim, J.; Rim, Y. S.; Chen, H.; Cao, H. H.; Nakatsuka, N.; Hinton, H. L.; Zhao, C.; Andrews.  
25 A. M.; Yang, Y.; Weiss, P. S. Fabrication of High-Performance Ultrathin In<sub>2</sub>O<sub>3</sub> Film Field-Effect  
26 Transistors and Biosensors Using Chemical Lift-Off Lithography. *ACS Nano* **2015**, *9*, 4572–  
27 4582.  
28  
29  
30  
31  
32  
33  
34 31. Andrews, A. M.; Liao, W.-S.; Weiss, P. S. Double-Sided Opportunities Using Chemical Lift-  
35 Off Lithography, *Acc. Chem. Res.* **2016**, *49*, 1449–1457.  
36  
37  
38  
39  
40 32. Monnell, J. D.; Stapleton, J. J.; Dirk, S. M.; Reinert, W. A.; Tour, J. M.; Allara, D. L.;  
41 Weiss, P. S. Relative Conductances of Alkaneselenolate and Alkanethiolate Monolayers on  
42 Au{111}. *J. Phys. Chem. B* **2005**, *109*, 20343–20349.  
43  
44  
45  
46  
47  
48 33. Zheng, Y. B.; Pathem, B. K.; Hohman, J. N.; Thomas, J. C.; Kim, M.; Weiss, P. S.  
49 Photoresponsive Molecules in Well-Defined Nanoscale Environments. *Adv. Mater.* **2013**, *25*,  
50 302–312.  
51  
52  
53



- 1  
2  
3 34. He, H.-X.; Huang, W.; Zhang, H.; Li, Q. G.; Li, S. F. Y.; Liu, Z. F. Demonstration of High-  
4 Resolution Capability of Chemical Force Titration *via* Study of Acid/Base Properties of a  
5 Patterned Self-Assembled Monolayer. *Langmuir* **2000**, *16*, 517–521.  
6  
7  
8  
9  
10  
11 35. Saavedra, H. M.; Thompson, C. M.; Hohman, J. N.; Crespi, V. H.; Weiss, P. S. Reversible  
12 Lability by *in Situ* Reaction of Self-Assembled Monolayers. *J. Am. Chem. Soc.* **2009**, *131*, 2252–  
13 2259.  
14  
15  
16  
17  
18  
19 36. Saavedra, H. M.; Mullen, T. J.; Zhang, P.; Dewey, D. C.; Claridge, S. A.; Weiss, P. S. Hybrid  
20 Strategies in Nanolithography. *Rep. Prog. Phys.* **2010**, *73*, 036501–036600.  
21  
22  
23  
24  
25 37. Saadi, F. H.; Carim, A. I.; Verlage, E.; Hemminger, J. C.; Lewis, N. S.; Soriaga, M. P. CoP  
26 as an Acid-Stable Active Electrocatalyst for the Hydrogen-Evolution Reaction: Electrochemical  
27 Synthesis, Interfacial Characterization and Performance Evaluation. *J. Phys. Chem. C* **2014**, *118*,  
28 29294–29300.  
29  
30  
31  
32  
33  
34  
35 38. Katano, S.; Kim, Y.; Matsubara, H.; Kitagawa, T.; Kawai, M. Hierarchical Chiral Framework  
36 Based on a Rigid Adamantane Tripod on Au(111). *J. Am. Chem. Soc.* **2007**, *129*, 2511–2515.  
37  
38  
39  
40 39. Hatzor, A.; McCarty, G. S.; D’Onofrio, T. G.; Fuchs, D. J.; Allara, D. L.; Tour, J. M.; Weiss,  
41 P. S. Scanning Tunneling Microscopy and Spectroscopy of Caltrops on Au{111}. Unpublished.  
42  
43  
44  
45  
46 40. Moore, A. M.; Dameron, A. A.; Mantooth, B. A.; Smith, R. K.; Fuchs, D. J.; Cizek, J. W.;  
47 Maya, F.; Yao, Y.; Tour, J. M.; Weiss, P. S. Molecular Engineering and Measurements to Test  
48 Hypothesized Mechanisms in Single Molecule Conductance Switching. *J. Am. Chem. Soc.* **2006**,  
49 *128*, 1959-1967.  
50  
51  
52  
53

- 1  
2  
3 41. Yao, Y.; Tour, J. M. Facile Convergent Route to Molecular Caltrops. *J. Org. Chem.* **1999**,  
4  
5 64, 1968–1971.  
6  
7  
8  
9 42. Jian, H.; Tour, J. M. En Route to Surface-Bound Electric Field-Driven Molecular Motors. *J.*  
10  
11 *Org. Chem.* **2003**, 68, 5091–5103.  
12  
13  
14 43. van Delden, R. A.; ter Wiel, M. K. J.; Pollard, M. M.; Vicario, J.; Koumura, N.; Feringa, B.  
15  
16 L. Unidirectional Molecular Motor on a Gold Surface. *Nature* **2005**, 437, 1337–1340.  
17  
18  
19  
20 44. Ye, T.; Kumar, A. S.; Saha, S.; Takami, T.; Huang, T. J.; Stoddart, J. F.; Weiss, P. S.  
21  
22 Changing Stations in Single Bistable Rotaxane Molecules under Electrochemical Control. *ACS*  
23  
24 *Nano* **2010**, 4, 3697–3701.  
25  
26  
27  
28 45. Donhauser, Z. J.; Mantooth, B. A.; Kelly, K. F.; Bumm, L. A.; Monnell, J. D.; Stapleton, J.  
29  
30 J.; Price, D. W. Jr.; Rawlett, A. M.; Allara, D. L.; Tour, J. M.; Weiss, P. S. Conductance  
31  
32 Switching in Single Molecules through Conformational Changes. *Science* **2001**, 292, 2303–2307.  
33  
34  
35  
36 46. Lewis, P. A.; Inman, C. E.; Maya, F.; Tour, J. M.; Hutchison, J. E.; Weiss, P. S. Molecular  
37  
38 Engineering of the Polarity and Interactions of Molecular Electronics Switches. *J. Am. Chem.*  
39  
40 *Soc.* **2005**, 127, 17421–17426.  
41  
42  
43  
44 47. Tersoff, J.; Hamann, D. R. Theory and Application for the Scanning Tunneling Microscope.  
45  
46 *Phys. Rev. Lett.* **1998**, 50, 1998–2001.  
47  
48  
49 48. McCarty, G. S.; Weiss, P. S. Scanning Probe Studies of Single Nanostructures. *Chem. Rev.*  
50  
51 **1999**, 99, 1983–1990.  
52  
53

- 1  
2  
3 49. Claridge, S. A.; Schwartz, J. J.; Weiss, P. S. Electrons, Photons, and Force: Quantitative  
4  
5 Single-Molecule Measurements from Physics to Biology. *ACS Nano* **2011**, *5*, 693–729.  
6  
7  
8  
9 50. Bonnell, D. A.; Basov, D. N.; Bode, M.; Diebold, U.; Kalinin, S. V.; Madhavan, V.;  
10  
11 Novotny, L.; Salmeron, M.; Schwarz, U. D.; Weiss, P. S. Imaging Physical Phenomena with  
12  
13 Local Probes: From Electrons to Photons. *Rev. Mod. Phys.* **2012**, *84*, 1343–1381.  
14  
15  
16  
17 51. Bumm, L. A.; Arnold, J. J.; Cygan, M. T.; Dunbar, T. D.; Burgin, T. P.; Jones, L., II; Allara,  
18  
19 D. L.; Tour, J. M.; Weiss, P. S. Are Single Molecular Wires Conducting? *Science* **1996**, *271*,  
20  
21 1705–1707.  
22  
23  
24  
25 52. Claridge, S. A.; Thomas, J. C.; Silverman, M. A.; Schwartz, J. J.; Yang, Y.; Wang, C.;  
26  
27 Weiss, P. S. Differentiating Amino Acid Residues and Side Chain Orientations in Peptides Using  
28  
29 Scanning Tunneling Microscopy. *J. Am. Chem. Soc.* **2013**, *135*, 18528–18535.  
30  
31  
32  
33 53. Moore, A. M.; Yeganeh, S.; Yao, Y.; Claridge, S. A.; Tour, J. M.; Ratner, M. A.; Weiss, P. S.  
34  
35 Polarizabilities of Adsorbed and Assembled Molecules: Measuring the Conductance through  
36  
37 Buried Contacts. *ACS Nano* **2010**, *4*, 7630–7636.  
38  
39  
40  
41 54. Thomas, J. C.; Goronzy, D. P.; Dragomeritskiy, K.; Zosso, D.; Gilles, J.; Osher, S. J.;  
42  
43 Bertozzi, A.; Weiss, P. S. Mapping Buried Hydrogen-Bonding Networks, *ACS Nano* **2016**, *10*,  
44  
45 5446–5451.  
46  
47  
48  
49 55. Yugay, D.; Goronzy, D. P.; Kawakami, L. M.; Claridge, S. A.; Song, T.-B.; Yan, Z.; Xie, Y.-  
50  
51 H.; Gilles, J.; Yang, Y.; Weiss, P. S. Copper Ion Binding Site in  $\beta$ -Amyloid Peptide. *Nano Lett.*  
52  
53 **2016**, *16*, 6282–6289.

- 1  
2  
3 56. Fujii, S.; Akiba, U.; Fujihira, M. Geometry for Self-Assembling of Spherical Hydrocarbon  
4 Cages with Methane Thiolates on Au(111). *J. Am. Chem. Soc.* **2002**, *124*, 13629–13635.  
5  
6  
7  
8  
9 57. Wade, K. The Structural Significance of the Number of Skeletal Bonding Electron-Pairs in  
10 Carboranes, the Higher Boranes and Borane Anions, and Various Transition-Metal Carbonyl  
11 Cluster Compounds. *J. Chem. Soc. D* **1971**, 792–793.  
12  
13  
14  
15  
16 58. Wiesendanger, R.; Eng, L.; Hidber, H. R.; Oelhafen, P.; Rosenthaler, L.; Stauer, U.;  
17 Güntherodt, H. J. Local Tunneling Barrier Height Images Obtained with the Scanning Tunneling  
18 Microscope. *Surf. Sci.* **1987**, *189–190*, 24–28.  
19  
20  
21  
22  
23  
24 59. Olesen, L.; Brandbyge, M.; Sørensen, M. R.; Jacobsen, K. W.; Lægsgaard, E.; Stensgaard, I.;  
25 Besenbacher, F. Apparent Barrier Height in Scanning Tunneling Microscopy Revisited. *Phys.*  
26 *Rev. Lett.* **1996**, *76*, 1485–1488.  
27  
28  
29  
30  
31  
32 60. Lang, N. D. Apparent Barrier Height in Scanning Tunneling Microscopy. *Phys. Rev. B* **1988**,  
33 *37*, 10395–10398.  
34  
35  
36  
37  
38 61. Jain, J.; Jain, A. Displacement Measurement and Its Application in Interframe Image Coding.  
39 *IEEE Trans. Comm.* **1981**, *29*, 1799–1808.  
40  
41  
42  
43 62. Love, N. S.; Kamath, C. An Empirical Study of Block Matching Techniques for the  
44 Detection of Moving Objects. *CASC, LLNL, Livermore* **2006**, 1–36.  
45  
46  
47  
48  
49 63. Slaughter, L. S.; Cheung, K. M.; Kaappa, S.; Cao, H. H.; Yang, Q.; Young, T. D.; Serino, A.  
50 C.; Malola, S.; Olson, J. M.; Link, S.; Häkkinen, H.; Andrews, A. M.; Weiss, P. S. Patterning  
51  
52  
53

- 1  
2  
3 Supported Gold Monolayers *via* Chemical Lift-Off Lithography. *Beilstein J. Nanotechnol.* **2017**,  
4  
5 8, 2648–2661.  
6  
7  
8  
9 64. Leites, L. A. Vibrational Spectroscopy of Carboranes and Parent Boranes and its Capabilities  
10  
11 in Carborane Chemistry. *Chem. Rev.* **1992**, *92*, 279–323.  
12  
13  
14 65. Stranick, S. J.; Parikh, A. N.; Allara, D. L.; Weiss, P. S. A New Mechanism for Surface  
15  
16 Diffusion: Motion of a Substrate-Adsorbate Complex. *J. Phys. Chem.* **1994**, *98*, 11136–11142.  
17  
18  
19  
20 66. Poirier, G. E.; Tarlov, M. J. Molecular Ordering and Gold Migration Observed in Butanethiol  
21  
22 Self-Assembled Monolayers using Scanning Tunneling Microscopy. *J. Phys. Chem.* **1995**, *99*,  
23  
24 10966–10970.  
25  
26  
27  
28 67. Kinbara, K.; Aida, T. Toward Intelligent Molecular Machines: Directed Motions of  
29  
30 Biological and Artificial Molecules and Assemblies, *Chem. Rev.* **2005**, *105*, 1377–1400.  
31  
32  
33  
34 68. Li, D.; Paxton, W. F.; Baughman, R. H.; Huang, T. J.; Stoddart, J. F.; Weiss, P. S. Molecular,  
35  
36 Supramolecular, and Macromolecular Motors and Artificial Muscles. *MRS Bull.* **2009**, *34*, 671–  
37  
38 681.  
39  
40  
41 69. Wang, J. Can Man-Made Nanomachines Compete with Nature Biomotors? *ACS Nano* **2009**, ,  
42  
43 4–9.  
44  
45  
46  
47 70. Abendroth, J. M.; Bushuyev, O. S.; Weiss, P. S.; Barrett, C. J. Controlling Motion at the  
48  
49 Nanoscale: Rise of the Molecular Machines. *ACS Nano* **2015**, *9*, 7746–7768.  
50  
51  
52  
53

- 1  
2  
3 71. Cheng, C.; McGonigal, P. R.; Stoddart, J. F.; Astumian, R. D. Design and Synthesis of  
4 Nonequilibrium Systems. *ACS Nano* **2015**, *9*, 8672–8688.  
5  
6  
7  
8  
9 72. Shimizu, T. K.; Jung, J.; Otani, T.; Han, Y.-K.; Kawai, M.; Kim Y. Two-Dimensional  
10 Superstructure Formation of Fluorinated Fullerene on Au(111): A Scanning Tunneling  
11 Microscopy Study. *ACS Nano* **2012**, *6*, 2679–2685.  
12  
13  
14  
15  
16  
17 73. Wiesboeck, R. A.; Hawthorne, M. F. Dicarbaundecaborane(13) and Derivatives. *J. Am.*  
18 *Chem. Soc.* **1964**, *86*, 1642–1643.  
19  
20  
21  
22 74. Bumm, L. A.; Arnold, J. J.; Charles, L. F.; Dunbar, T. D.; Allara, D. L.; Weiss, P. S. Directed  
23 Self-Assembly to Create Molecular Terraces with Molecularly Sharp Boundaries in Organic  
24 Monolayers. *J. Am. Chem. Soc.* **1999**, *121*, 8017–8021.  
25  
26  
27  
28  
29  
30 75. Ferris, J. H.; Kushmerick, J. G.; Johnson, J. A.; Yoshikawa Youngquist, M. G.; Kessinger, R.  
31 B.; Kingsbury, H. F.; Weiss, P. S. Design, Operation, and Housing of an Ultrastable, Low  
32 Temperature, Ultrahigh Vacuum Scanning Tunneling Microscope. *Rev. Sci. Instrum.* **1998**, *69*,  
33 2691–2695.  
34  
35  
36  
37  
38  
39  
40 76. Moulder, J. F. *Handbook of X-ray Photoelectron Spectroscopy: A Reference Book of*  
41 *Standard Spectra for Identification and Interpretation of XPS Data*; Perkin-Elmer Corporation,  
42 Physical Electronics Division: Eden Prairie, MN, 1992.  
43  
44  
45  
46  
47  
48 77. Kresse, G.; Hafner, J. *Ab Initio* Molecular Dynamics for Liquid Metals. *Phys. Rev. B.* **1993**,  
49 *47*, 558–561.  
50  
51  
52  
53

- 1  
2  
3 78. Kresse, G.; Hafner, J. *Ab Initio* Molecular-Dynamics Simulation of the Liquid-Metal-  
4 Amorphous-Semiconductor Transition in Germanium. *Phys. Rev. B* **1994**, 49,14251–14269.  
5  
6  
7  
8  
9 79. Kresse, G.; Furthmüller, J. Efficiency of *Ab-Initio* Total Energy Calculations for Metals and  
10 Semiconductors Using a Plane-Wave Basis Set. *Comput. Mat. Sci.* **1996**, 6, 15–50.  
11  
12  
13  
14 80. Kresse, G.; Furthmüller, J. Efficient Iterative Schemes for *Ab Initio* Total-Energy  
15 Calculations Using a Plane-Wave Basis Set. *Phys. Rev. B.* **1996**, 54, 11169–11186.  
16  
17  
18  
19  
20 81. Perdew, J. P.; Burke, K.; Ernzerhof, M. Generalized Gradient Approximation Made Simple  
21 *Phys. Rev. Lett.* **1997**, 78, 1396–3868.  
22  
23  
24  
25  
26 82. Kresse, G.; Joubert, D. From Ultrasoft Pseudopotentials to the Projector Augmented-Wave  
27 Method. *Phys. Rev. B* **1999**, 59, 1758–1775.  
28  
29  
30  
31 83. Grimme, S.; Antony, J.; Ehrlich, S; Krieg, S. A consistent and Accurate *Ab Initio*  
32 Parametrization of Density Functional Dispersion Correction (DFT-D) for the 94 elements H-Pu.  
33 *J. Chem. Phys.* **2010**, 132, 154104–154122.  
34  
35  
36  
37  
38  
39 84. Dunnington, B. D.; & Schmidt, J. R. Generalization of Natural Bond Orbital Analysis to  
40 Periodic Systems: Applications to Solids and Surfaces *via* Plane-Wave Density Functional  
41 Theory. *J. Chem. Theory Comput.* **2012**, 8, 1902–1911.  
42  
43  
44  
45  
46  
47 85. Weigend, F. Accurate Coulomb-Fitting Basis Sets for H to Rn, *Phys. Chem. Chem. Phys.*  
48 **2006**, 8, 1057–1065.  
49  
50  
51  
52  
53

1  
2  
3 86. Weigend, F.; Ahlrichs, R. Balanced Basis Sets of Split Valence, Triple Zeta Valence and  
4  
5  
6 Quadruple Zeta Valence Quality for H to Rn: Design and Assessment of Accuracy, *Phys. Chem.*  
7  
8 *Chem. Phys.* **2005**, 7, 3297–3305.  
9  
10  
11  
12  
13  
14  
15  
16  
17  
18  
19  
20  
21  
22  
23  
24  
25  
26  
27  
28  
29  
30  
31  
32  
33  
34  
35  
36  
37  
38  
39  
40  
41  
42  
43  
44  
45  
46  
47  
48  
49  
50  
51  
52  
53



Table of Contents and Abstract Graphic

